

Article

Supported Nanostructured Mo_xC Materials for the Catalytic Reduction of CO₂ through the Reverse Water Gas Shift Reaction

Arturo Pajares ^{1,2,†} , Xianyun Liu ^{1,‡}, Joan R. Busacker ¹, Pilar Ramírez de la Piscina ¹ and Narcís Homs ^{1,2,*}

¹ Departament de Química Inorgànica i Orgànica, Secció de Química Inorgànica & Institut de Nanociència i Nanotecnologia (IN2UB), Universitat de Barcelona, Martí i Franquès 1, 08028 Barcelona, Spain

² Catalonia Institute for Energy Research (IREC), Jardins de les Dones de Negre 1, 08930 Barcelona, Spain

* Correspondence: nhoms@irec.cat or narcis.homs@qi.ub.edu

† Present address: Sustainable Materials Management, Flemish Institute for Technological Research (VITO NV), Boeretang 200, 2400 Mol, Belgium.

‡ Present address: College of Chemistry and Chemical Engineering, Henan Polytechnic University, Jiaozuo 454003, China.

Abstract: Mo_xC-based catalysts supported on γ-Al₂O₃, SiO₂ and TiO₂ were prepared, characterized and studied in the reverse water gas shift (RWGS) at 548–673 K and atmospheric pressure, using CO₂:H₂ = 1:1 and CO₂:H₂ = 1:3 mol/mol reactant mixtures. The support used determined the crystalline Mo_xC phases obtained and the behavior of the supported nanostructured Mo_xC catalysts in the RWGS. All catalysts were active in the RWGS reaction under the experimental conditions used; CO productivity per mol of Mo was always higher than that of unsupported Mo₂C prepared using a similar method in the absence of support. The CO selectivity at 673 K was above 94% for all the supported catalysts, and near 99% for the SiO₂-supported. The Mo_xC/SiO₂ catalyst, which contains a mixture of hexagonal Mo₂C and cubic MoC phases, exhibited the best performance for CO production.

Keywords: CO₂ catalytic reduction; syngas; RWGS; supported molybdenum carbide; Mo_xC-based catalysts



Citation: Pajares, A.; Liu, X.; Busacker, J.R.; Ramírez de la Piscina, P.; Homs, N. Supported Nanostructured Mo_xC Materials for the Catalytic Reduction of CO₂ through the Reverse Water Gas Shift Reaction. *Nanomaterials* **2022**, *12*, 3165. <https://doi.org/10.3390/nano12183165>

Academic Editors: Fabrizio Pirri and James Evans

Received: 27 July 2022

Accepted: 9 September 2022

Published: 13 September 2022

Publisher's Note: MDPI stays neutral with regard to jurisdictional claims in published maps and institutional affiliations.



Copyright: © 2022 by the authors. Licensee MDPI, Basel, Switzerland. This article is an open access article distributed under the terms and conditions of the Creative Commons Attribution (CC BY) license (<https://creativecommons.org/licenses/by/4.0/>).

1. Introduction

In addition to capture and storage of CO₂, nowadays there is a clear interest in its use as an out-stream chemical feedstock in order to actively contribute to the reduction of CO₂ emissions; CO₂ can be considered a cheap carbon C1 source for upgrading rather than a waste with consequences in global warming [1–4]. However, the direct transformation of CO₂ to useful products is difficult. The high chemical stability of CO₂ difficult its catalytic transformation, the developing of new materials capable of efficiently bind and activate this molecule is nowadays an active research area. An interesting CO₂ utilization approach is its reduction to CO, employing H₂ as a reducing agent via the reverse water gas shift (RWGS) reaction [5–8]:



The reduction of CO₂ to CO with renewable H₂ can be regarded as a simple and easy path for CO₂ recycling, which would allow its reuse at a large scale. After the RWGS step and H₂O separation, a CO₂/CO/H₂ out-stream mixture can be produced. This out-stream can be used as syngas input for other well-established chemical processes, such as Fischer-Tropsch (FT) or methanol synthesis [9–15].

The RWGS reaction can be carried out using noble metal-based catalysts [5,10,16]. Due to the similar properties of transition metal carbides (TMCs) and Pt-based catalysts, the formers have been proposed as catalysts for different processes in which Pt-based catalysts are active [17,18]. One of these processes is the CO₂ reduction to CO, which has been analyzed over different TMCs using theoretical and experimental approaches [19–25].

The preparation of TMCs is usually carried out using carburization methods. These methods apply high temperature and/or pressure conditions in the presence of a reducing atmosphere, usually mixtures of H_2 and carbon-containing gases (CO , CH_4 , C_2H_4) [25–28]. Due to the increased interest in TMC-based catalysts, in recent years, greener preparation methods have been explored [21,22,29–31]. In an earlier investigation, we studied the preparation of bulk Mo_xC catalysts using different molybdenum and carbon precursors and following sol-gel based routes; the bulk Mo_xC catalysts generated, contained different crystalline phases, which influenced their catalytic behavior in the RWGS reaction [31].

The deposition onto a support of the appropriate TMC active phase can be an interesting approach to improve the catalytic behavior of bulk TMCs materials, which usually show low surface area values. Supported Mo_xC phases have been used as catalysts in different processes such as CH_4 dry reforming [32], hydrazine decomposition [33], thiophene hydrodesulfurization [34], propene and tetralin hydrogenation [35] and Fischer-Tropsch synthesis [36]. However, supported Mo_xC catalysts have not been much studied in the RWGS reaction [37–39]. Porosoff et al. have reported the promoter effect of K in Al_2O_3 -supported Mo_2C -based catalysts containing MoO_2 and/or metallic Mo, which were prepared by carburization with CH_4/H_2 at 873 K [38]. Sub-nanosized molybdenum carbide clusters highly dispersed onto N-doped carbon/ Al_2O_3 , prepared by carbonization of MoO_3 with glucose, were more performant in the RWGS than bulk β - Mo_2C [39]. Recently, the preparation of SiO_2 - and SBA-15-supported Mo_2C -based catalysts (20% wt Mo), using different routes of Mo incorporation to the support and a final carburization process with CH_4/H_2 , has been studied [40]. The preparation method and the support influenced the composition of Mo_xC_y crystalline phases developed and therefore the catalytic performance of the material in the RWGS [40]. The preparation of Mo_xC -based catalysts supported onto γ - Al_2O_3 , SiO_2 and MFI-type zeolites by incipient wetness impregnation of ammonium molybdate and carburization with CH_4/H_2 , have led to catalysts with different Mo-containing species such as Mo_2C , MoO_3 and Mo^0 ; the phases developed and the catalytic performance in the RWGS of the materials depended also on the support characteristics [41].

Here, Mo_xC phases were generated onto γ - Al_2O_3 , SiO_2 and TiO_2 by a thermal treatment of the solid obtained from the interaction between a $MoCl_5$ /urea solution and the corresponding oxide. The crystalline Mo_xC phases obtained depended on the support used in the preparation and determined the catalytic behavior of materials in the RWGS.

2. Experimental

2.1. Preparation of Catalysts

Commercial γ - Al_2O_3 (Alfa Aesar, Haverhill, MA, US, $226\text{ m}^2\text{ g}^{-1}$), SiO_2 (Degussa, Frankfurt, Germany, $200\text{ m}^2\text{ g}^{-1}$) and TiO_2 (Tecnan, Navarra, Spain, $117\text{ m}^2\text{ g}^{-1}$, anatase/rutile, 78/22% wt) were employed as supports. Urea (Alfa Aesar, Haverhill, MA, US, 99%), which was used as carbon source, was added to a solution of $MoCl_5$ (Alfa Aesar, Haverhill, MA, US, 99.6%) in ethanol with a urea/ $MoCl_5$ = 7 molar ratio [21,29,31]. The viscous solution was contacted with the respective powdered support. The resulting solid was dried at 333 K, and then treated under Ar flow up to 1073 K for 3 h. The samples were cooled down to room temperature under Ar and then exposed to air without passivation. Mo_xC/Al_2O_3 , Mo_xC/TiO_2 and Mo_xC/SiO_2 catalysts with about 26% wt of Mo were prepared by using the proper amount of molybdenum and carbon precursors. A reference catalyst (unsupported), containing only bulk hexagonal Mo_2C was prepared following a similar method but in the absence of support [21]. For characterization purposes, the commercial supports were also separately treated up to 1073 K (3 h) under Ar.

2.2. Characterization of Catalysts

The Mo content of samples was determined by inductively coupled plasma mass spectrometry using a Perkin Elmer Optima 3200RL apparatus (Santa Clara, CA, US). The N_2 adsorption-desorption isotherms were recorded at 77 K using a Micromeritics Tristar II 3020 equipment. Prior to the measurements, the samples were outgassed at 523 K for

5 h. The specific surface area (S_{BET}) was calculated by multi-point BET analysis of N_2 adsorption isotherms. The X-ray powder diffraction (XRD) analysis was performed using a PANalytical X'Pert PRO MPD Alpha1 powder diffractometer (Malvern, UK) equipped with a $\text{CuK}\alpha_1$ radiation. The XRD profiles were collected in the 2θ range of 4° – 100° with a step size of 0.017° and counting 50 s at each step. Transmission electron microscopy (TEM-HRTEM) images and energy dispersive X-ray analysis (EDX) were collected employing a JEOL J2010F microscope (Tokyo, Japan) operated at an accelerating voltage to 200 kV. The Raman spectra of the samples were collected using a Jobin-Yvon LabRam HR 800, fitted to an optical Olympus BXFM microscope (Kyoto, Japan) with a 532 nm laser and a CCD detector. X-ray photoelectron spectroscopy (XPS) analysis was performed using a Perkin Elmer PHI-5500 Multitechnique System (Physical Electronics, Chanhassen, MN, US) with an Al X-ray source ($h\nu = 1486.6$ eV and 350 W). Samples were kept in an ultra-high vacuum chamber during data acquisition ($5 \cdot 10^{-9}$ – $2 \cdot 10^{-8}$ Torr). Before XPS measurements, the C 1s BE of adventitious carbon was determined in the same equipment and conditions using Au as reference. The BE values were referred to the mentioned C 1s BE at 284.8 eV.

2.3. RWGS Catalytic Tests

The RWGS reaction tests were carried out in a Microactivity-Reference unit (PID Eng&Tech) using a tubular fixed-bed reactor under atmospheric pressure. Approximately, 150 mg of catalyst were diluted with inactive SiC up to 1 mL of catalytic bed. The RWGS was studied at 0.1 MPa, between 548 K and 673 K, by following the temperature sequence: 598 K (3 h)→573 K (3 h)→548 K (10 h)→598 K (3 h)→623 K (3 h)→648 K (3 h)→673 K (3 h)→648 K (5 h). The first part of the catalytic test: 598 K (3 h)→573 K (3 h)→548 K (10 h) was carried out in order to condition the catalyst under RWGS. The gas hourly space velocity (GHSV) was 3000 h^{-1} . The effluent was analysed on-line with a gas chromatograph Varian 450-GC equipped with a methanizer and TCD and FID detectors. CO_2 conversion and product distribution at each temperature were determined by the average of at least three measures.

3. Results and Discussion

As stated above, Al_2O_3 -, SiO_2 - and TiO_2 -supported Mo_xC catalysts with about 26% wt Mo were prepared, characterized and tested in the RWGS reaction. Table 1 shows the Mo content and the S_{BET} of fresh catalysts. For comparison, S_{BET} values of the supports treated at 1073 K under Ar, which are the conditions used in the preparation of catalysts, are also included. In all cases, the S_{BET} of the supports after the thermal treatment at 1073 K was lower than that of the corresponding commercial pristine material; the diminution was about 10% for Al_2O_3 and SiO_2 , meanwhile for TiO_2 the S_{BET} decreased from $117 \text{ m}^2\text{g}^{-1}$ to $13 \text{ m}^2\text{g}^{-1}$. For TiO_2 , a phase change occurred during the thermal treatment; the rutile weight percentage increased from 22% (pristine material) until 95% after the treatment at 1073 K, as determined from XRD analysis [42]. On the other hand, except for the $\text{Mo}_x\text{C}/\text{TiO}_2$, the S_{BET} of supported catalysts was lower than that of the corresponding support treated at 1073 K; the formation of Mo_xC could prevent in some extension the surface area decrease of the TiO_2 support, which could be related with a different extent of the rutile formation from anatase.

Table 1. Mo content, determined by chemical analysis and surface area (S_{BET}) of fresh and post-reaction catalysts.

Catalyst	Mo (%wt)	S_{BET} ($\text{m}^2 \text{g}^{-1}$)		
		Fresh ^a	Post-Reaction ^b	Post-Reaction ^c
$\text{Mo}_x\text{C}/\text{Al}_2\text{O}_3$	25.1	119 (204)	93	97
$\text{Mo}_x\text{C}/\text{SiO}_2$	25.5	129 (181)	115	107
$\text{Mo}_x\text{C}/\text{TiO}_2$	27.5	39 (13)	32	25

^a between brackets S_{BET} of supports treated at 1073 K; ^b $\text{CO}_2/\text{H}_2/\text{N}_2 = 1/3/1$ reactant mixture; ^c $\text{CO}_2/\text{H}_2/\text{N}_2 = 1/1/3$ reactant mixture.

The supported catalysts were analyzed by XRD, and the corresponding XRD patterns are shown in Figures 1–3; XRD patterns of the respective supports treated at 1073 K under Ar are also displayed for comparison. From the XRD pattern of $\text{Mo}_x\text{C}/\text{Al}_2\text{O}_3$ (Figure 1), characteristic diffraction peaks of $\gamma\text{-Al}_2\text{O}_3$ are observed, and the main presence of hexagonal Mo_2C (JCPDS 00-035-0787) can be deduced; a crystallite size of 28 nm was calculated. The XRD analysis of $\text{Mo}_x\text{C}/\text{SiO}_2$ (Figure 2) indicates the presence of hexagonal Mo_2C ; however, the observation of diffraction peaks with maxima at $2\theta = 36.9^\circ$ and $2\theta = 42.1^\circ$ are attributed to the presence of cubic MoC (JCPDS 03-065-0280). From the intensity of diffraction peaks of both phases and that in reference files, a semiquantitative analysis was performed [43]; the presence of 65% cubic MoC and 35% hexagonal Mo_2C is determined in the $\text{Mo}_x\text{C}/\text{SiO}_2$ catalyst. Figure 3 shows the corresponding XRD profile of TiO_2 -supported catalyst. Characteristic diffraction peaks of both anatase and rutile TiO_2 phases are clearly observed. The rutile weight percentage with respect to TiO_2 phases calculated from XRD pattern is 51% [42]. As commented above, the formation of Mo_xC could prevent the anatase transformation, having the $\text{Mo}_x\text{C}/\text{TiO}_2$ catalyst a higher amount of anatase and a higher surface area than the support treated at 1073 K (Table 1). From the XRD pattern of $\text{Mo}_x\text{C}/\text{TiO}_2$, the main presence of cubic MoC with poor crystallinity can be proposed, even if the presence of hexagonal Mo_2C could not be ruled out (Figure 3).

The catalysts were also characterized by Raman spectroscopy, TEM-HRTEM, STEM-EDX and XPS. Raman spectroscopy was used in order to determine the presence of molybdenum oxide species and/or carbonaceous residues (Figure S1). The very low intensity bands in the zone $815\text{--}990\text{ cm}^{-1}$ points to the presence of residual MoO_3 [44–46], which could be formed by surface oxidation when the samples were exposed to air. For $\text{Mo}_x\text{C}/\text{TiO}_2$, Raman bands at $260, 429$ and 610 cm^{-1} , assigned to rutile, and at 150 cm^{-1} assigned to anatase, are clearly visible [47–49]. In all cases, the intensity of the bands in the $1200\text{--}1700\text{ cm}^{-1}$ region characteristic of carbonaceous species (D and G bands), is negligible (Figure S1).

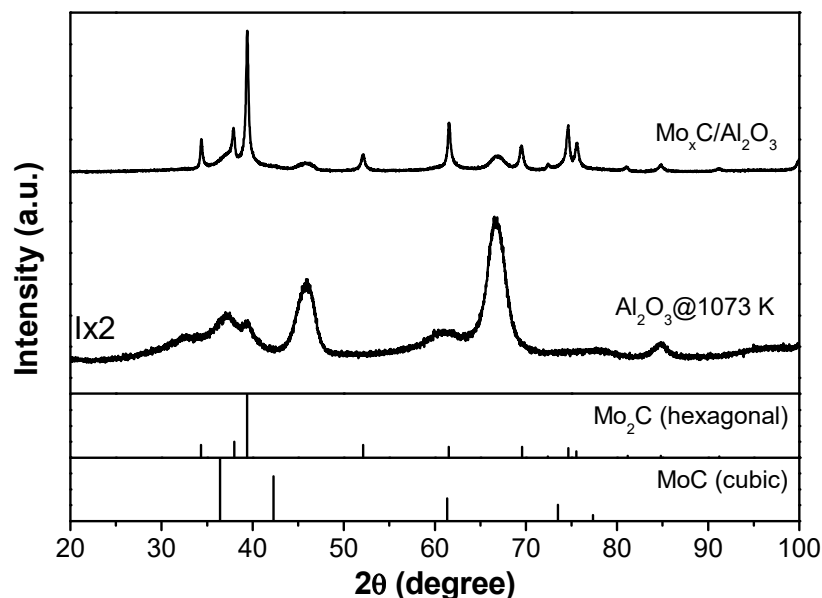


Figure 1. XRD patterns of $\text{Mo}_x\text{C}/\text{Al}_2\text{O}_3$ catalyst and the Al_2O_3 support after thermal treatment at 1073 K.

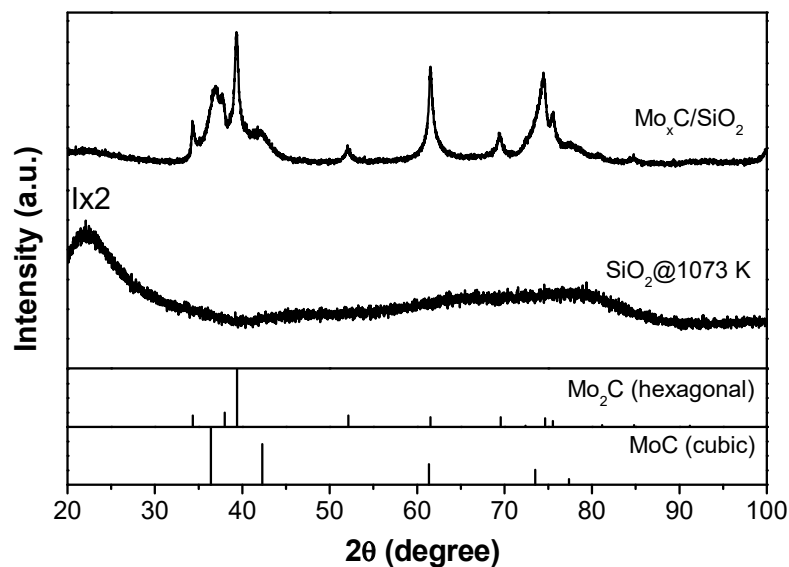


Figure 2. XRD patterns of $\text{Mo}_x\text{C}/\text{SiO}_2$ catalyst and the SiO_2 support after thermal treatment at 1073 K.

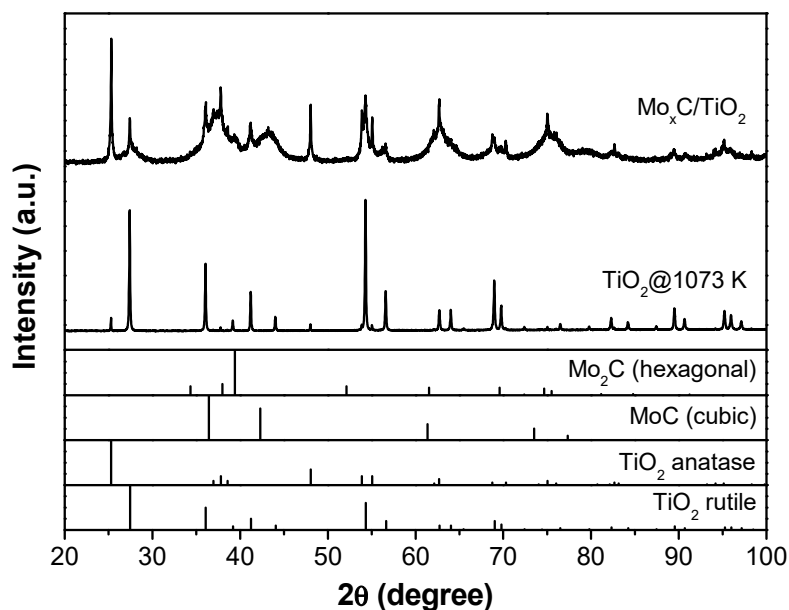


Figure 3. XRD patterns of $\text{Mo}_x\text{C}/\text{TiO}_2$ catalyst and the TiO_2 support after thermal treatment at 1073 K.

TEM-HRTEM and STEM-EDX analysis of $\text{Mo}_x\text{C}/\text{Al}_2\text{O}_3$, $\text{Mo}_x\text{C}/\text{SiO}_2$ and $\text{Mo}_x\text{C}/\text{TiO}_2$ are shown in Figures 4–6, respectively. For $\text{Mo}_x\text{C}/\text{Al}_2\text{O}_3$ (Figure 4), the presence of hexagonal Mo_2C with a mean particle size of 21 nm was determined in agreement with XRD results. TEM-HRTEM analysis of $\text{Mo}_x\text{C}/\text{SiO}_2$ (Figure 5) allowed to confirm the presence of hexagonal Mo_2C and cubic MoC particles with bimodal distribution and mean particle sizes of 18 nm and 5 nm, respectively (Figure 5A–C). For $\text{Mo}_x\text{C}/\text{TiO}_2$ (Figure 6), only the presence of the cubic MoC phase with a mean particle size of 4 nm could be determined. The supported Mo_xC materials studied in this work follow the recently predicted general trend of size-dependent phase diagrams for bulk Mo and W carbides: fcc phases are generally found at small particle size and hcp phases are prevalent at large particle size [50].

In all cases, STEM-EDX results (see Figures 4C, 5D, and 6C) indicate a homogeneous distribution of Mo on the corresponding support. Figures 4D, 5E and 6D, show the corresponding EDX spectra; N- and Cl-containing species were not detected.

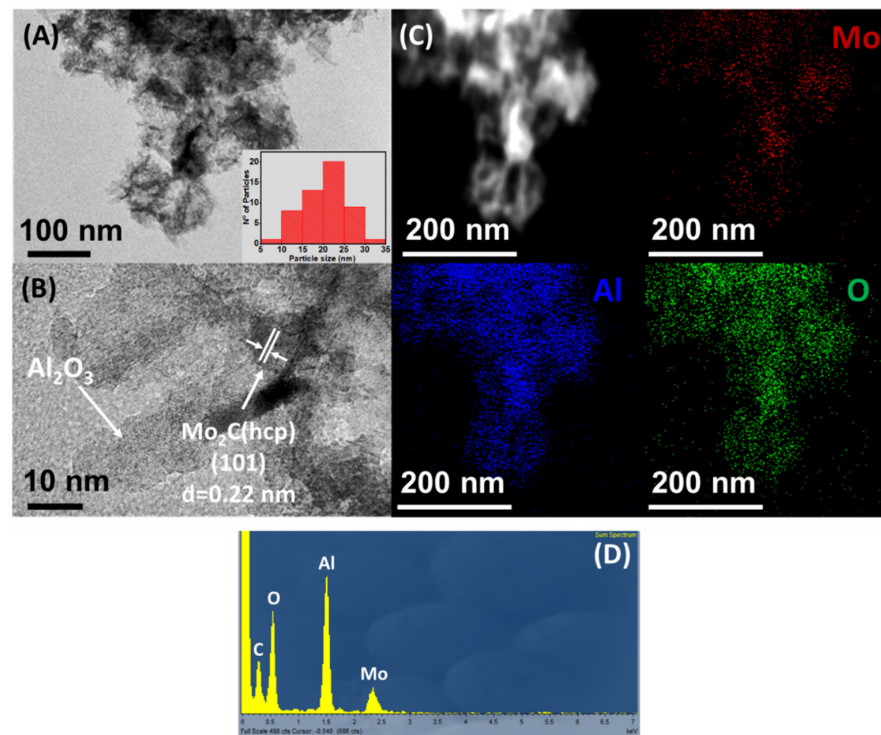


Figure 4. (A,B) TEM–HRTEM micrographs of $\text{Mo}_x\text{C}/\text{Al}_2\text{O}_3$ catalyst; (C) STEM–EDX mapping; (D) EDX spectrum.

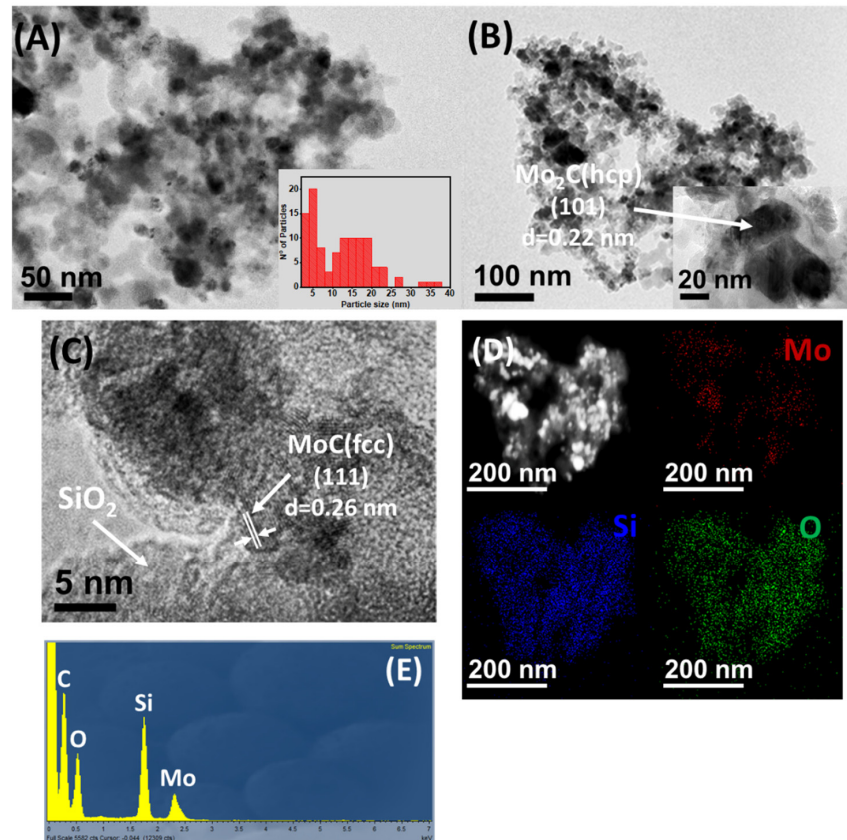


Figure 5. (A–C) TEM–HRTEM micrographs of $\text{Mo}_x\text{C}/\text{SiO}_2$ catalyst; (D) STEM–EDX mapping; (E) EDX spectrum.

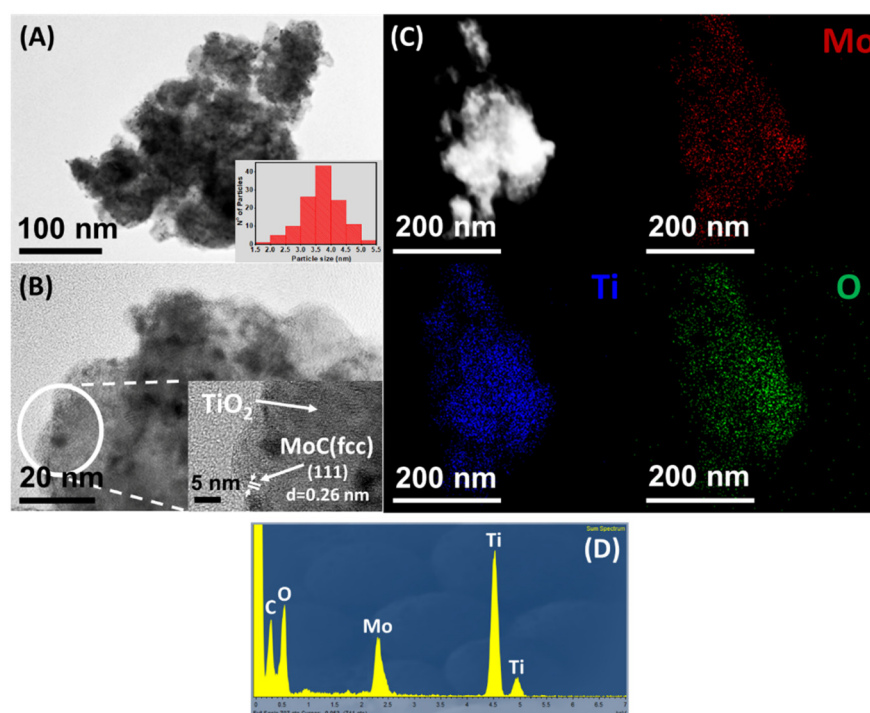


Figure 6. (A,B) TEM–HRTEM micrographs of $\text{Mo}_x\text{C}/\text{TiO}_2$ catalyst; (C) STEM–EDX mapping; (D) EDX spectrum.

As stated above, the catalysts were also analyzed by XPS. Al 2p, Si 2p and Ti 2p_{3/2} BE at 74.8, 104.0 and 459.3 eV, characteristic of Al₂O₃, SiO₂, and TiO₂, were found for Mo_xC/Al₂O₃, Mo_xC/SiO₂ and Mo_xC/TiO₂, respectively (Figure S2). Figure 7 shows the C 1s and Mo 3d XP spectra. The C 1s core level spectra (Figure 7A) show a maximum at 284.8 eV associated to the adventitious carbon, the component at 283.7–283.8 eV is associated to surface molybdenum carbide species [21,31,51–54]. Components extended above 284.8 eV are related to different oxygen containing species [52–56]. The Mo 3d spectra are complex (Figure 7B); however, they can be deconvoluted into four doublets (Mo 3d_{5/2} and Mo 3d_{3/2}). According to literature, the Mo 3d_{5/2}/Mo 3d_{3/2} intensity ratio was fixed to be 1.5, and the Mo 3d_{5/2}–Mo 3d_{3/2} BE splitting was set at 3.1 eV [57–59]. The 3d_{5/2} peaks at the lowest BE region, 228.5–228.7 eV, are attributed to Mo²⁺ and Mo³⁺ in Mo₂C and/or oxycarbide species [19,21,31,51]. The Mo 3d_{5/2} components at 229.4–229.5, 231.3–232.6 and 233.2 eV, can be assigned to Mo⁴⁺, Mo⁵⁺ and Mo⁶⁺ surface species, respectively [19,58–61], which could be related to the presence of MoC, oxycarbide and/or oxide species. Table 2 shows the contribution of Mo²⁺/Mo³⁺ and Mo⁴⁺ species to the total surface Moⁿ⁺ species; the Mo_xC/SiO₂ catalyst having both Mo₂C and MoC shows the highest values.

Table 2. Apparent E_a determined for Mo_xC/support catalysts and surface characteristics determined from XPS.

Catalyst	E _a (kJ·mol ^{−1})	(Mo ^{2+,3+} /Total Mo ⁿ⁺) _{XPS}	(Mo ^{2+,3+,4+} /Total Mo ⁿ⁺) _{XPS}
Mo _x C/Al ₂ O ₃	77.7 ± 1.7	0.277	0.347
Mo _x C/SiO ₂	64.9 ± 3.2	0.431	0.690
Mo _x C/TiO ₂	77.9 ± 4.1	0.098	0.316

Reaction conditions: CO₂/H₂/N₂ = 1/1/3, GHSV = 3000 h^{−1}, P = 0.1 MPa and T = 598–648 K.

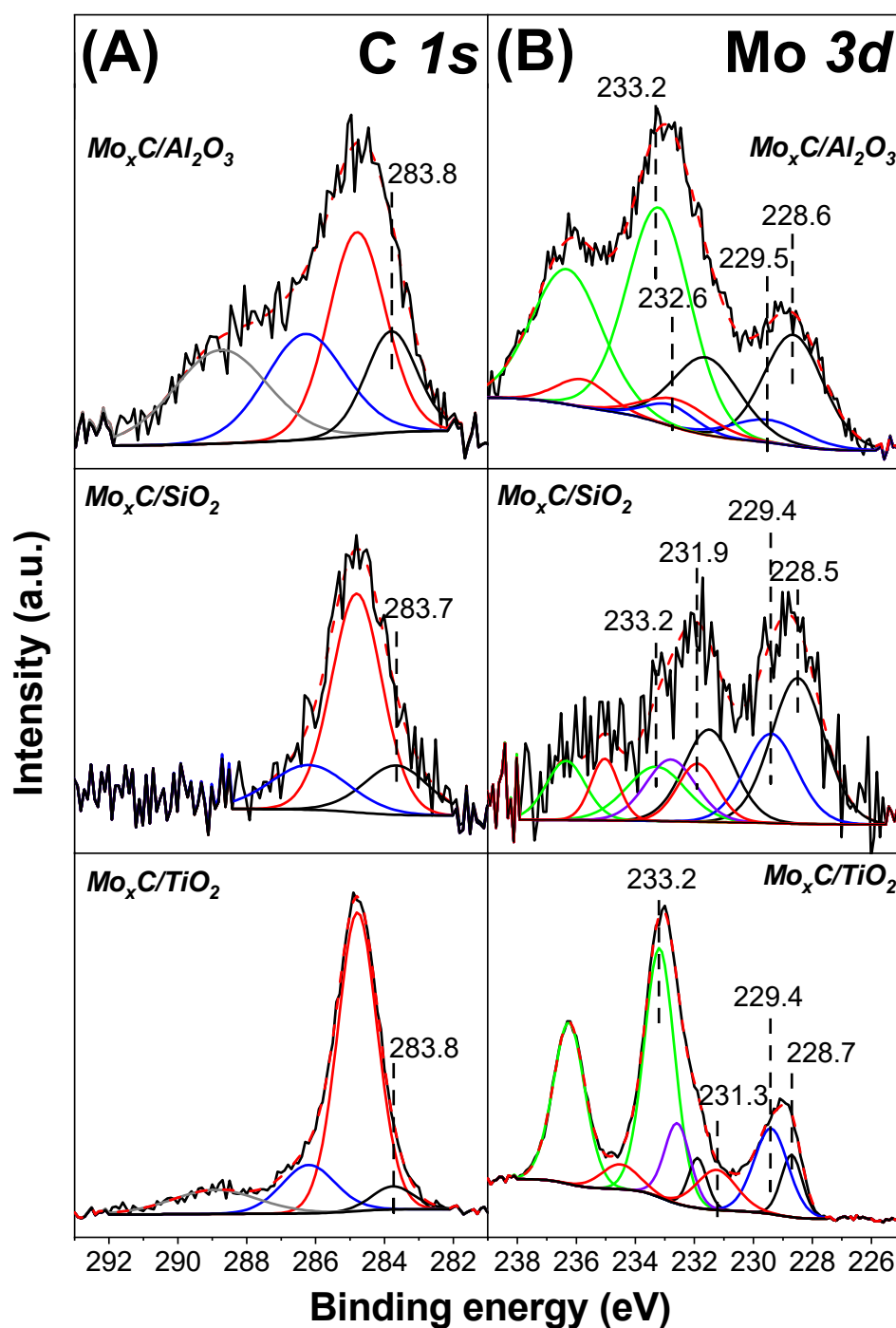


Figure 7. XPS spectra of $\text{Mo}_x\text{C}/\text{support}$ catalysts: (A) C 1s level; (B) Mo 3d level.

All catalysts were tested in the RWGS using $\text{CO}_2:\text{H}_2 = 1/3$ and $\text{CO}_2/\text{H}_2 = 1/1$ ratios. Catalytic data of unsupported Mo_2C , prepared using a similar method to that used in this work but in the absence of support, are also included for comparison [21]. As stated in the experimental section, the first part of the catalytic test: 598 K (3 h) \rightarrow 573 K (3 h) \rightarrow 548 K (10 h) was carried out in order to condition the catalyst under RWGS. Next, when the temperature was increased to 598 K, the CO_2 conversion was in all cases higher than that obtained at 598 K in the conditioning step (Figure 8A and Figure 10A). This behavior could be related with the removal of initially adsorbed surface species. After this first step and regardless the catalyst and the conditions, CO_2 conversion increases with the rising of reaction temperature from 598 K to 673 K (Figure 8A and Figure 10A).

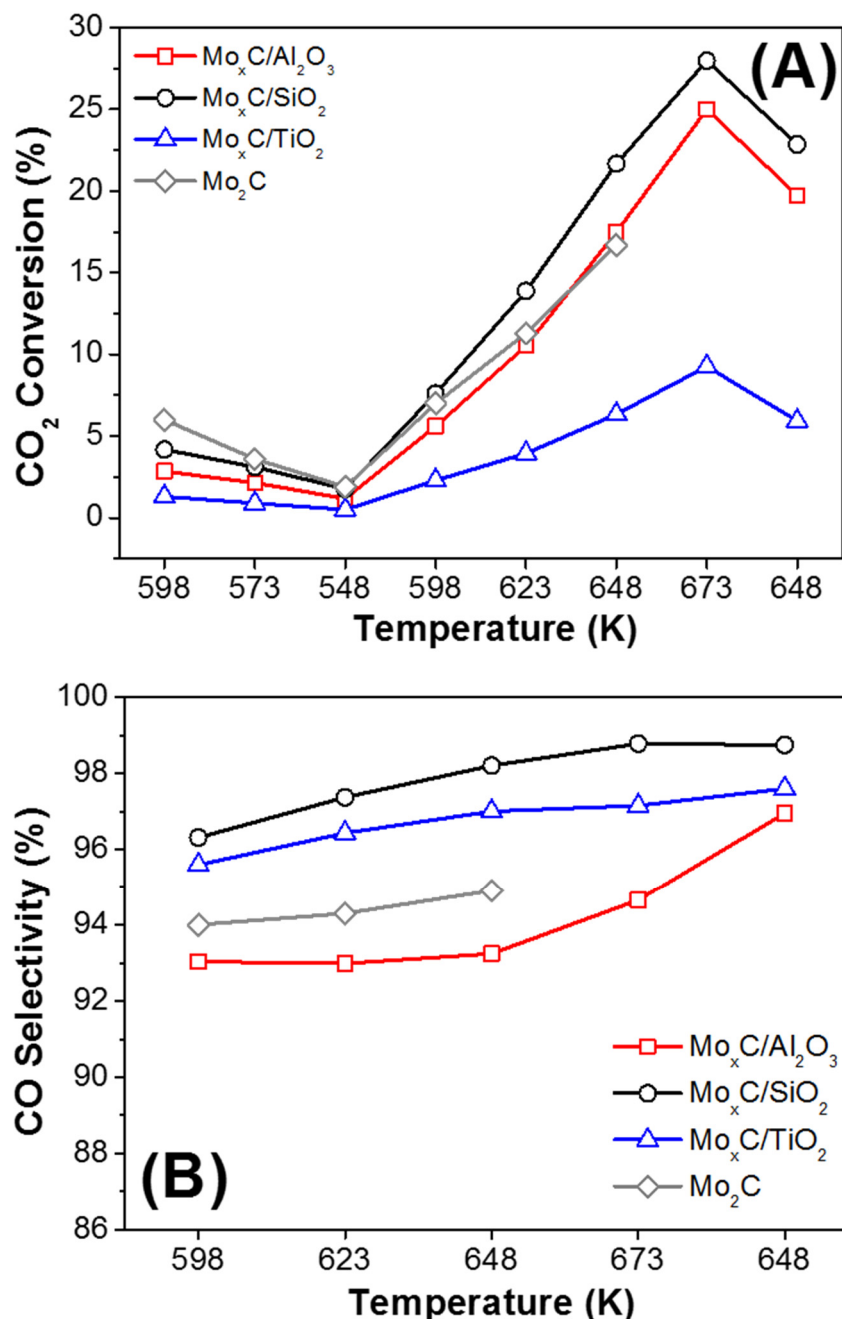


Figure 8. Catalytic behavior of $\text{Mo}_x\text{C}/\text{support}$ and unsupported reference Mo_2C catalysts in the RWGS reaction as a function of reaction temperature; (A) CO_2 conversion, (B) CO selectivity. Reaction conditions: $m_{\text{cat}} = 150$ mg, $\text{CO}_2/\text{H}_2/\text{N}_2 = 1/3/1$, GHSV = 3000 h⁻¹, $P = 0.1$ MPa.

Figures 8 and 9 show the RWGS behavior of catalysts when $\text{CO}_2:\text{H}_2 = 1/3$ is used. $\text{Mo}_x\text{C}/\text{SiO}_2$ presented the highest value of CO_2 conversion (27.5%) at 673 K (Figure 8A); the corresponding equilibrium CO_2 conversion for RWGS at the experimental conditions used is about 37% (at 673 K). $\text{Mo}_x\text{C}/\text{Al}_2\text{O}_3$ showed a catalytic activity close to that of the unsupported Mo_2C catalyst. Meanwhile, $\text{Mo}_x\text{C}/\text{TiO}_2$ showed lower values of CO_2 conversion than those of unsupported Mo_2C [21]. These results contrast with those usually reported for supported metallic catalysts [62,63]. The activity of SiO_2 - and Al_2O_3 -supported metals in the RWGS is usually lower than that found when reducible supports such as TiO_2 or CeO_2 are used, which can generate oxygen vacancies that strengthens the CO_2 adsorption and then the activity in the RWGS [63]. In this work, besides the difference in the surface-

area of catalysts, the composition and characteristics of generated Mo_xC nanoparticles change as a function of the support.

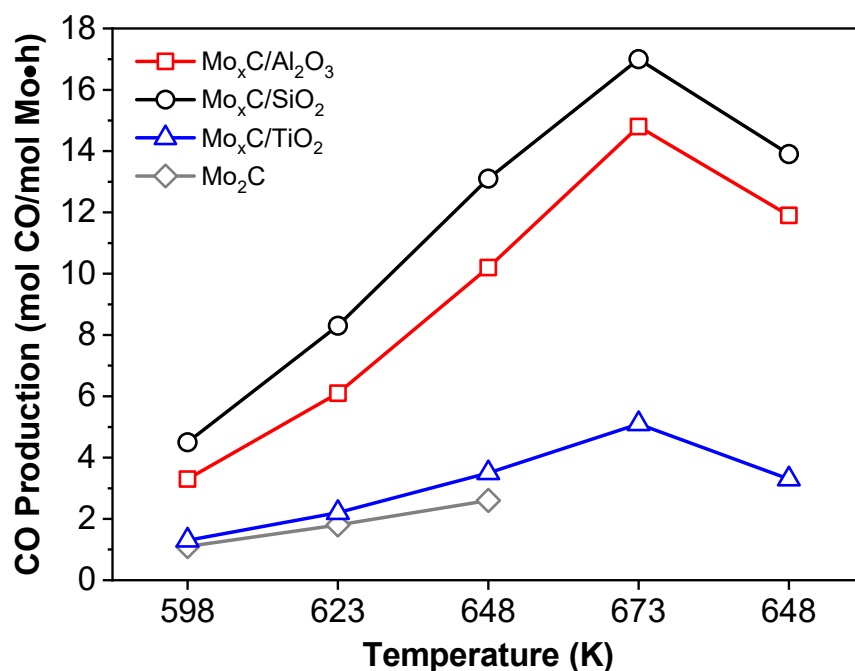


Figure 9. CO production per mol of Mo as a function of reaction temperature in RWGS over $\text{Mo}_x\text{C}/\text{support}$ and unsupported reference Mo_2C catalysts. Reaction conditions: $m_{\text{cat}} = 150$ mg, $\text{CO}_2/\text{H}_2/\text{N}_2 = 1/3/1$, $\text{GHSV} = 3000$ h^{-1} , $P = 0.1$ MPa.

A key process in the RWGS is the cleavage of C-O bond with $\text{CO} + \text{O}$ formation. In this context molybdenum oxycarbide has been proposed as an intermediate in the RWGS over Mo_2C that likely enhances the RWGS rate [25]. We have demonstrated that over a polycrystalline $\alpha\text{-Mo}_2\text{C}$ catalyst, prepared with the method used in the present work, the enhanced CO_2 dissociation toward $\text{CO} + \text{O}$ results from specific surface facets [21]. Next, the easy release of CO and the continuous O removal by H_2 to form H_2O , results in high RWGS activity. The existence of both, hcp Mo_2C and fcc MoC phases in the SiO_2 -supported catalyst, could result in interphases regions with appropriate characteristics to enhance RWGS on $\text{Mo}_x\text{C}/\text{SiO}_2$ catalyst. In this context, for different Mo_xC bulk catalysts, the lowest activation energy in the RWGS was found for a catalyst containing several Mo_2C and MoC phases [31].

All the supported catalysts showed high CO selectivity values. When $\text{CO}_2:\text{H}_2 = 1/3$ was used, CO selectivity were always higher than 92% (Figure 8B). The highest CO selectivity was observed for the $\text{Mo}_x\text{C}/\text{SiO}_2$ catalyst, achieving at 673 K, 98.5%. Only $\text{Mo}_x\text{C}/\text{Al}_2\text{O}_3$ showed CO selectivity values slightly lower than that of unsupported Mo_2C (Figure 8B). CH_4 was the main byproduct and only very small amounts of ethylene were formed.

For a proper comparison of the catalysts, the values of CO production were calculated per mol of Mo in the samples; results are shown in Figure 9. All the supported catalysts showed a higher CO production per mol of Mo compared to the unsupported Mo_2C catalyst [21]. At the end of the catalytic test, $\text{Mo}_x\text{C}/\text{SiO}_2$ and $\text{Mo}_x\text{C}/\text{Al}_2\text{O}_3$ showed a higher CO production at 648 K than before reaction at 673 K (Figure 9). This could be related with the removal of remaining oxygen surface species during the reaction at 673 K. The highest CO production in the whole range of reaction temperature tested was obtained for $\text{Mo}_x\text{C}/\text{SiO}_2$; it reached about 17.0 mol CO/mol Mo·h at 673 K.

Catalysts were also tested in the RWGS using a stoichiometric ratio of the reactant mixture, $\text{CO}_2/\text{H}_2/ = 1/1$. Figure 10 shows the variation of CO_2 conversion and CO selectivity values. As expected, the CO_2 conversion (Figure 10A) was lower and the CO

selectivity (Figure 10B) higher when a mixture $\text{CO}_2/\text{H}_2 = 1/1$ was used than when the reactant mixture was $\text{CO}_2/\text{H}_2 = 1/3$. Using the $\text{CO}_2/\text{H}_2 = 1/1$ reactant mixture, the highest CO_2 conversion (Figure 10A) and the highest CO production per mol of Mo (Figure 11), in the whole range of reaction temperature tested, were also found over the $\text{Mo}_x\text{C}/\text{SiO}_2$ catalyst. In this case, at the end of the catalytic test, only for $\text{Mo}_x\text{C}/\text{SiO}_2$ a slightly higher CO production at 648 K than before reaction at 673 K was observed (Figure 11).

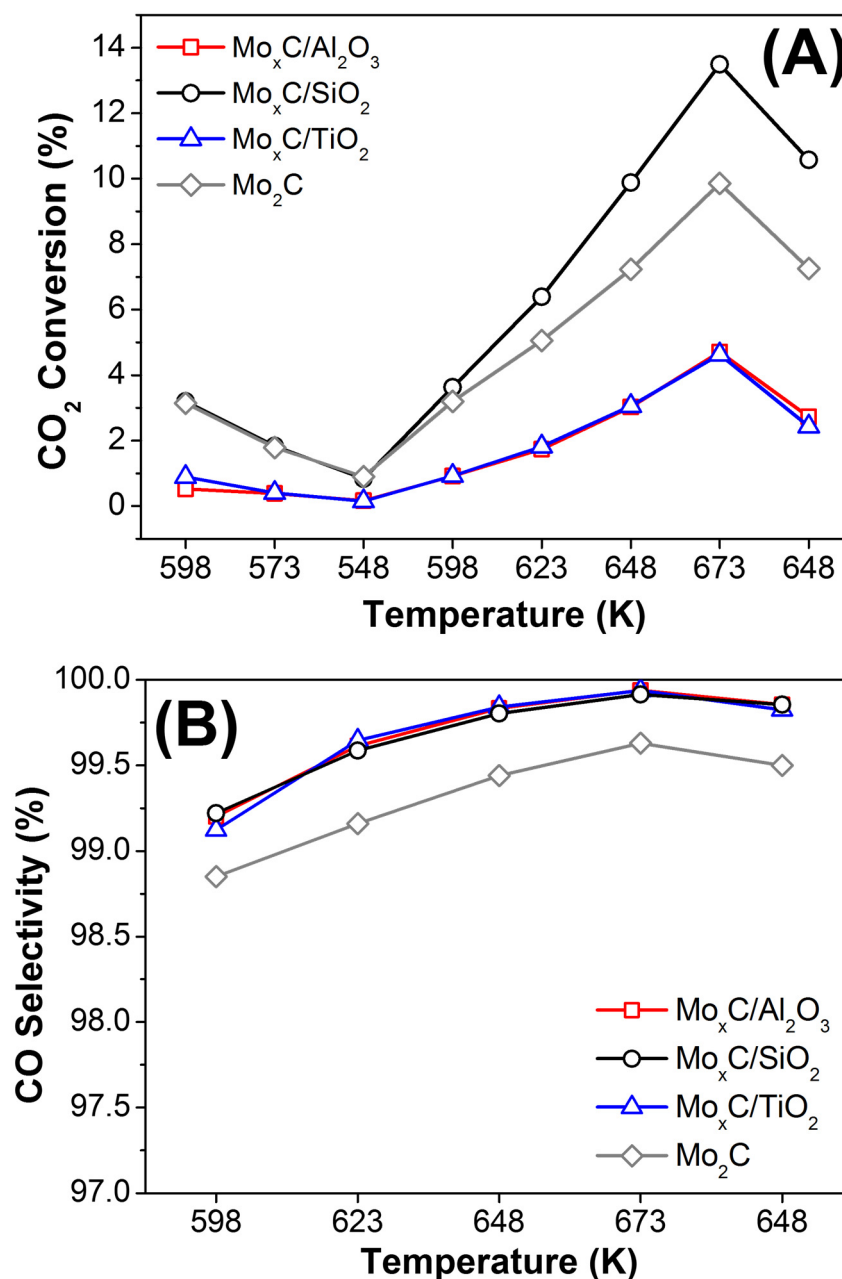


Figure 10. Catalytic behavior of $\text{Mo}_x\text{C}/\text{support}$ and unsupported reference Mo_2C catalysts in the RWGS reaction as a function of reaction temperature; (A) CO_2 conversion, (B) CO selectivity. Reaction conditions: $m_{\text{cat}} = 150$ mg, $\text{CO}_2/\text{H}_2/\text{N}_2 = 1/1/3$, GHSV = 3000 h^{-1} , $P = 0.1$ MPa.

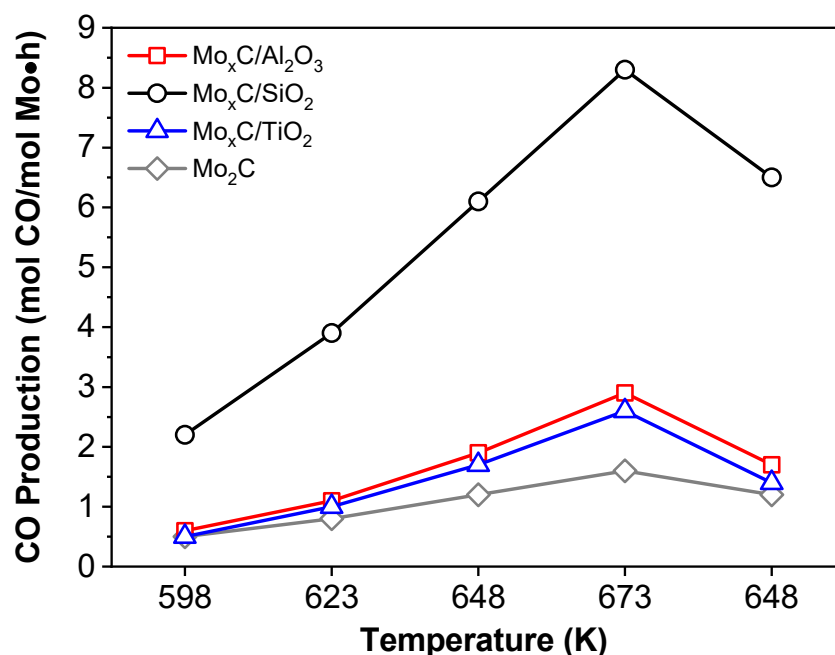


Figure 11. CO production per mol Mo as a function of reaction temperature in RWGS over Mo_xC/support and unsupported reference Mo₂C catalysts. Reaction conditions: $m_{\text{cat}} = 150$ mg, $\text{CO}_2/\text{H}_2/\text{N}_2 = 1/1/3$, GHSV = 3000 h^{-1} , $P = 0.1$ MPa.

It is noteworthy, that after the overall RWGS study carried out, all supported catalysts, showed quite constant values of CO₂ conversion and CO selectivity during the last step at 648 K (5 h), under both $\text{CO}_2/\text{H}_2 = 1/3$ and $\text{CO}_2/\text{H}_2 = 1/1$ conditions.

The apparent activation energies (E_a) for CO production over supported catalysts were calculated according to the Arrhenius plots in the temperature range of 598–648 K; values between 65–78 kJ/mol were obtained (Table 2). These values are in the range of that recently reported for an alumina supported Mo₂C cluster-based catalyst (76.4 kJ/mol) [39]. Mo_xC/SiO₂ showed the lowest E_a for CO production. As stated above, the best performance of Mo_xC/SiO₂ could be related with the coexistence in this catalyst of different Mo_xC phases, hexagonal Mo₂C and cubic MoC, as has been recently suggested for unsupported Mo_xC catalysts [31]. Moreover, Mo_xC/SiO₂ showed the highest contribution of Mo²⁺/Mo³⁺ and Mo⁴⁺ species to the total surface Moⁿ⁺ species. For Mo_xC-based catalysts, an easy reduction under reaction conditions of molybdenum species has been related with their performance in RWGS [41].

Post-reaction catalysts were characterized by BET and XRD. Only a slight decrease in the BET surface area was found after the RWGS reaction (Table 1). The XRD patterns of fresh (Figures 1–3) and post-reaction catalysts after the test with $\text{CO}_2/\text{H}_2 = 1/3$ (Figure S3) were similar. Meanwhile, the presence of MoO₂ was detected by XRD in post-reaction Mo_xC/SiO₂ and Mo_xC/TiO₂ when the reactant mixture was $\text{CO}_2/\text{H}_2 = 1/1$ (Figure S4); the oxidation could be prevented under a richer hydrogen atmosphere ($\text{CO}_2/\text{H}_2 = 1/3$) due to an easier removal of the O surface species formed from the CO₂ activation over these materials under $\text{CO}_2/\text{H}_2 = 1/3$ conditions [21,31].

4. Conclusions

Using urea and MoCl₅ as carbon and molybdenum sources, different Mo_xC phases were successfully supported over Al₂O₃, SiO₂ and TiO₂. The support determined the developed Mo_xC phases on the materials and their catalytic behavior in the RWGS. Hexagonal Mo₂C nanoparticles on Mo_xC/Al₂O₃ and cubic MoC nanoparticles on Mo_xC/TiO₂ were found. Over Mo_xC/SiO₂ both hexagonal Mo₂C and cubic MoC nanoparticles were present. In all cases, supported hexagonal Mo₂C nanoparticles were larger than cubic MoC ones.

All catalysts showed a stable catalytic behavior and exhibited higher CO production per mol of Mo than the unsupported hexagonal Mo₂C similarly prepared, under the reaction conditions used (CO₂/H₂ = 1/3 and CO₂/H₂ = 1/1; T = 548–673 K).

Mo_xC/SiO₂ exhibited the highest surface ratio of Mo species with low oxidation states (Mo^{2+,3+,4+}) and the best performance in the RWGS reaction. Over Mo_xC/SiO₂, CO₂ conversion of 27.5% and CO selectivity of 98.5% were achieved at 673 K under CO₂/H₂ = 1/3; for CO production, an apparent activation energy of 64.9 ± 3.2 kJ mol⁻¹ was determined at 598–648 K under CO₂/H₂ = 1/1. The catalytic behavior is proposed to be governed by the supported Mo_xC phase. The simultaneous presence of hexagonal Mo₂C and cubic MoC nanoparticles in Mo_xC/SiO₂ plays a main role on the catalytic behavior of this catalyst.

Supplementary Materials: The following supporting information can be downloaded at: <https://www.mdpi.com/article/10.3390/nano12183165/s1>, Figure S1. Raman spectra of fresh Mo_xC/support catalysts; Figure S2. XP spectra of Mo_xC/support catalysts. (A) Al 2p level registered for Mo_xC/Al₂O₃, (B) Si 2p level registered for Mo_xC/SiO₂, (C) Ti 2p level registered for Mo_xC/TiO₂; Figure S3. XRD patterns of Mo_xC/support catalysts after RWGS reaction (CO₂/H₂ = 1/3); reaction conditions: m_{cat} = 150 mg, GHSV = 3000 h⁻¹, P = 0.1 MPa.; Figure S4. XRD patterns of Mo_xC/support catalysts after RWGS reaction (CO₂/H₂ = 1/1); reaction conditions: m_{cat} = 150 mg, GHSV = 3000 h⁻¹, P = 0.1 MPa.

Author Contributions: Methodology, experimental and formal analysis A.P., X.L., J.R.B., P.R.d.I.P. and N.H.; writing—original draft, A.P., X.L., P.R.d.I.P. and N.H.; writing—review and editing, A.P., P.R.d.I.P. and N.H.; supervision, P.R.d.I.P. and N.H.; project administration and funding acquisition, P.R.d.I.P. and N.H. All authors have read and agreed to the published version of the manuscript.

Funding: This research was funded by MAT2017-87500-P and PID2020-116031RB I00/AEI/10.13039/501100011033/FEDER projects.

Institutional Review Board Statement: Not applicable.

Informed Consent Statement: Not applicable.

Data Availability Statement: The data present in this study are available on request from the corresponding author.

Acknowledgments: The authors thank MAT2017-87500-P and PID2020-116031RB I00/AEI/10.13039/501100011033/FEDER projects, for financial support. J.R.B. acknowledges the Spanish SECAT for his master thesis grant. X.L. is grateful to the China Scholarship Council and the University of Barcelona (IN2UB) for her PhD grants. A.P. thanks MINECO for his PhD grant (BES-C-2015-074574).

Conflicts of Interest: The authors declare no conflict of interest.

References

1. Leung, D.Y.C.; Caramanna, G.; Maroto-Valer, M.M. An Overview of Current Status of Carbon Dioxide Capture and Storage Technologies. *Renew. Sustain. Energy Rev.* **2014**, *39*, 426–443. [[CrossRef](#)]
2. Cuéllar-Franca, R.M.; Azapagic, A. Carbon Capture, Storage and Utilisation Technologies: A Critical Analysis and Comparison of Their Life Cycle Environmental Impacts. *J. CO₂ Util.* **2015**, *9*, 82–102. [[CrossRef](#)]
3. Choi, S.; Drese, J.H.; Jones, C.W. Adsorbent Materials for Carbon Dioxide Capture from Large Anthropogenic Point Sources. *Chem. Sus. Chem.* **2009**, *2*, 796–854. [[CrossRef](#)] [[PubMed](#)]
4. D'Alessandro, D.M.; Smit, B.; Long, J.R. Carbon Dioxide Capture: Prospects for New Materials. *Angew. Chem. Int. Ed. Engl.* **2010**, *49*, 6058–6082. [[CrossRef](#)] [[PubMed](#)]
5. Homs, N.; Toyir, J.; Ramirez de la Piscina, P. Catalytic Processes for Activation of CO₂. In *New and Future Developments in Catalysis*; Elsevier: Amsterdam, The Netherlands, 2013; pp. 1–26.
6. Din, I.U.; Shaharun, M.S.; Alotaibi, M.A.; Alharthi, A.I.; Naeem, A. Recent Developments on Heterogeneous Catalytic CO₂ Reduction to Methanol. *J. CO₂ Util.* **2019**, *34*, 20–33.
7. Saeidi, S.; Najari, S.; Hessel, V.; Wilson, K.; Keil, F.J.; Concepción, P.; Suib, S.L.; Rodrigues, A.E. Recent Advances in CO₂ Hydrogenation to Value-Added Products—Current Challenges and Future Directions. *Prog. Energy Combust.* **2021**, *85*, 100905.
8. Bahmanpour, A.M.; Signorile, M.; Kröcher, O. Recent Progress in Syngas Production Via Catalytic CO₂ Hydrogenation Reaction. *Appl. Catal. B* **2021**, *295*, 120319. [[CrossRef](#)]

9. Boot-Handford, M.E.; Abanades, J.C.; Anthony, E.J.; Blunt, M.J.; Brandani, S.; Mac Dowell, N.; Fernández, J.R.; Ferrari, M.C.; Gross, R.; Hallett, J.P.; et al. Carbon Capture and Storage Update. *Energy Environ. Sci.* **2014**, *7*, 130–189.
10. Daza, Y.A.; Kuhn, J.N. CO₂ Conversion by Reverse Water Gas Shift Catalysis: Comparison of Catalysts, Mechanisms and Their Consequences for CO₂ Conversion to Liquid Fuels. *RSC Adv.* **2016**, *6*, 49675–49691. [[CrossRef](#)]
11. Liu, X.M.; Lu, G.Q.; Yan, Z.F.; Beltramini, J. Recent Advances in Catalysts for Methanol Synthesis Via Hydrogenation of CO and CO₂. *Ind. Eng. Chem. Res.* **2003**, *42*, 6518–6530. [[CrossRef](#)]
12. Jahangiri, H.; Bennett, J.; Mahjoubi, P.; Wilson, K.; Gu, S. A Review of Advanced Catalyst Development for Fischer–Tropsch Synthesis of Hydrocarbons from Biomass Derived Syn-Gas. *Catal. Sci. Technol.* **2014**, *4*, 2210–2229. [[CrossRef](#)]
13. Saeidi, S.; Amin, N.A.S.; Rahimpour, M.R. Hydrogenation of CO₂ to Value-Added Products—A Review and Potential Future Developments. *J. CO₂ Util.* **2014**, *5*, 66–81. [[CrossRef](#)]
14. Elsernagawy, O.Y.H.; Hoadley, A.; Patel, J.; Bhatelia, T.; Lim, S.; Haque, N.; Li, C. Thermo-Economic Analysis of Reverse Water-Gas Shift Process With Different Temperatures for Green Methanol Production as a Hydrogen Carrier. *J. CO₂ Util.* **2020**, *41*, 101280. [[CrossRef](#)]
15. Kirsch, H.; Sommer, U.; Pfeifer, P.; Dittmeyer, R. Power-To-Fuel Conversion Based on Reverse Water-Gas-Shift, Fischer-Tropsch Synthesis and Hydrocracking: Mathematical Modeling and Simulation in Matlab/Simulink. *Chem. Eng. Sci.* **2020**, *227*, 115930. [[CrossRef](#)]
16. Liang, B.; Duan, H.; Su, X.; Chen, X.; Huang, Y.; Chen, X.; Delgado, J.J.; Zhang, T. Promoting Role of Potassium in the Reverse Water Gas Shift Reaction on Pt/Mullite Catalyst. *Catal. Today* **2017**, *281*, 319–326. [[CrossRef](#)]
17. Levy, R.B.; Boudart, M. Platinum-Like Behavior of Tungsten Carbide in Surface Catalysis. *Science* **1973**, *181*, 547–549. [[CrossRef](#)] [[PubMed](#)]
18. Oyama, S.T. *The Chemistry of Transition Metal Carbides and Nitrides*; Blackie Academic & Professional: Glasgow, Scotland, 1996.
19. Porosoff, M.D.; Yang, X.; Boscoboinik, J.A.; Chen, J.G. Molybdenum Carbide as Alternative Catalysts to Precious Metals for Highly Selective Reduction of CO₂ to CO. *Angew. Chem. Int. Ed. Engl.* **2014**, *53*, 6705–6709. [[CrossRef](#)]
20. Porosoff, M.D.; Kattel, S.; Li, W.; Liu, P.; Chen, J.G. Identifying Trends and Descriptors for Selective CO₂ Conversion to CO Over Transition Metal Carbides. *Chem. Commun.* **2015**, *51*, 6988–6991. [[CrossRef](#)]
21. Liu, X.; Kunkel, C.; Ramírez de la Piscina, P.; Homs, N.; Viñes, F.; Illas, F. Effective and Highly Selective CO Generation from CO₂ Using a Polycrystalline α -Mo₂C Catalyst. *ACS Catal.* **2017**, *7*, 4323–4335. [[CrossRef](#)]
22. Pajares, A.; Prats, H.; Romero, A.; Viñes, F.; de la Piscina, P.; Sayós, R.; Homs, N.; Illas, F. Critical Effect of Carbon Vacancies on the Reverse Water Gas Shift Reaction over Vanadium Carbide Catalysts. *Appl. Catal. B* **2020**, *267*, 118719. [[CrossRef](#)]
23. Kunkel, C.; Viñes, F.; Illas, F. Transition metal carbides as novel materials for CO₂ capture, storage, and activation. *Energy Environ. Sci.* **2016**, *9*, 141–144. [[CrossRef](#)]
24. Posada-Pérez, S.; Viñes, F.; Ramirez, P.J.; Vidal, A.B.; Rodriguez, J.A.; Illas, F. The bending machine: CO₂ activation and hydrogenation on δ -MoC(001) and β -Mo₂C(001) surfaces. *Phys. Chem. Chem. Phys.* **2014**, *16*, 14912–14921. [[CrossRef](#)] [[PubMed](#)]
25. Reddy, K.P.; Dama, S.; Mhamane, N.B.; Ghosalya, M.K.; Raja, T.; Satyanarayana, C.V.; Gopinath, C.S. Molybdenum carbide catalyst for the reduction of CO₂ to CO: Surface science aspects by NAPPES and catalysis studies. *Dalton Trans.* **2019**, *48*, 12199–12209. [[CrossRef](#)]
26. Claridge, J.B.; York, A.P.E.; Brungs, A.J.; Green, M.L.H. Study of the Temperature-Programmed Reaction Synthesis of Early Transition Metal Carbide and Nitride Catalyst Materials from Oxide Precursors. *Chem. Mater.* **2000**, *12*, 132–142. [[CrossRef](#)]
27. Volpe, L.; Boudart, M. Compounds of Molybdenum and Tungsten with High Specific Surface Area. *J. Solid State Chem.* **1985**, *59*, 348–356. [[CrossRef](#)]
28. Naito, S.; Tsuji, M.; Sakamoto, Y.; Miyao, T. Marked Difference of Catalytic Behavior by Preparation Methods in CH₄ Reforming with CO₂ Over Mo₂C and WC Catalysts. *Stud. Surf. Sci. Catal.* **2000**, *143*, 415–423.
29. Giordano, C.; Erpen, C.; Yao, W.; Antonietti, M. Synthesis of Mo and W Carbide and Nitride Nanoparticles Via a Simple “Urea Glass” Route. *Nano Lett.* **2008**, *8*, 4659–4663. [[CrossRef](#)]
30. Gao, J.; Wu, Y.; Jia, C.; Zhong, Z.; Gao, F.; Yang, Y.; Liu, B. Controllable Synthesis of α -MoC_{1-x} and β -Mo₂C Nanowires for Highly Selective CO₂ Reduction to CO. *Catal. Commun.* **2016**, *84*, 147–150. [[CrossRef](#)]
31. Liu, X.; Pajares, A.; Matienzo, D.D.C.; Ramírez de la Piscina, P.; Homs, N. Preparation and Characterization of Bulk Mo_xC Catalysts and Their Use in the Reverse Water-Gas Shift Reaction. *Catal. Today* **2020**, *356*, 384–389. [[CrossRef](#)]
32. Tsuji, M.; Miyao, T.; Naito, S. Remarkable Support Effect of ZrO₂ Upon the CO₂ Reforming of CH₄ Over Supported Molybdenum Carbide Catalysts. *Catal. Lett.* **2000**, *60*, 195–198. [[CrossRef](#)]
33. Chen, X.; Zhang, T.; Ying, P.; Zheng, M.; Wu, W.; Xia, L.; Li, T.; Wang, X.; Li, C. A Novel Catalyst for Hydrazine Decomposition: Molybdenum Carbide Supported on γ -Al₂O₃. *Chem. Commun.* **2002**, *3*, 288–289. [[CrossRef](#)] [[PubMed](#)]
34. Aegerter, P.A.; Quigley, W.W.C.; Simpson, G.J.; Ziegler, D.D.; Logan, J.W.; McCrea, K.R.; Glazier, S.; Bussell, M.E. Thiophene Hydrodesulfurization over Alumina-Supported Molybdenum Carbide and Nitride Catalysts: Adsorption Sites, Catalytic Activities, and Nature of the Active Surface. *J. Catal.* **1996**, *164*, 109–121. [[CrossRef](#)]
35. Da Costa, P.; Potvin, C.; Manoli, J.M.; Breyse, M.; Djéga-Mariadassou, G. Novel Phosphorus-Doped Alumina-Supported Molybdenum and Tungsten Carbides: Synthesis, Characterization and Hydrogenation Properties. *Catal. Lett.* **2001**, *72*, 91–97. [[CrossRef](#)]

36. Vo, D.N.; Adesina, A.A. Fischer–Tropsch Synthesis over Alumina-Supported Molybdenum Carbide Catalyst. *Appl. Catal. A Gen.* **2011**, *399*, 221–232. [[CrossRef](#)]
37. Nagai, M.; Kurakami, T. Reverse Water Gas Shift Reaction Over Molybdenum Carbide. *J. Chem. Eng. Jpn.* **2005**, *38*, 807–812. [[CrossRef](#)]
38. Porosoff, M.D.; Baldwin, J.W.; Peng, X.; Mpourmpakis, G.; Willauer, H.D. Potassium-Promoted Molybdenum Carbide as a Highly Active and Selective Catalyst for CO₂ Conversion to CO. *Chem. Sus. Chem.* **2017**, *10*, 2408–2415. [[CrossRef](#)] [[PubMed](#)]
39. Ma, Y.; Guo, Z.; Jiang, Q.; Wu, K.; Gong, H.; Liu, Y. Molybdenum Carbide Clusters for Thermal Conversion of CO₂ to CO Via Reverse Water-Gas Shift Reaction. *J. Energy Chem.* **2020**, *50*, 37–43. [[CrossRef](#)]
40. Marquart, W.; Raseale, S.; Prieto, G.; Zimina, A.; Sarma, B.B.; Grunwaldt, J.-D.; Claeys, M.; Fischer, N. CO₂ Reduction over Mo₂C-Based Catalysts. *ACS Catal.* **2021**, *11*, 1624–1639. [[CrossRef](#)]
41. Juneau, M.; Pope, C.; Liu, R.; Porosoff, M.D. Support Acidity as a Descriptor for Reverse Water-Gas Shift over Mo₂C-Based Catalysts. *Appl. Catal. A Gen.* **2021**, *620*, 118034. [[CrossRef](#)]
42. Zhang, H.; Banfield, J.F. Understanding Polymorphic Phase Transformation Behavior During Growth of Nanocrystalline Aggregates: Insights from TiO₂. *J. Phys. Chem. B* **2000**, *104*, 3481–3487. [[CrossRef](#)]
43. Snyder, R.L. The use of reference intensity ratios in X-ray quantitative analysis. *Powder Diffr.* **1992**, *7*, 186–193. [[CrossRef](#)]
44. Dieterle, M.; Weinberg, G.; Mestl, G. Raman Spectroscopy of Molybdenum Oxides. Part I. Structural Characterization of Oxygen Defects in MoO_{1-x} by DR UV/VIS, Raman Spectroscopy and X-Ray Diffraction. *Phys. Chem. Chem. Phys.* **2002**, *4*, 812–821. [[CrossRef](#)]
45. Silveira, J.V.; Batista, J.A.; Saraiva, G.D.; Mendes Filho, J.; Souza Filho, A.G.; Hu, S.; Wang, X. Temperature Dependent Behavior of Single Walled MoO₃ Nanotubes: A Raman Spectroscopy Study. *Vib. Spectrosc.* **2010**, *54*, 179–183. [[CrossRef](#)]
46. Camacho-López, M.; Escobar-Alarcón, L.; Picquart, M.; Arroyo, R.; Córdoba, G.; Haro-Poniatowski, E. Micro-Raman Study of the m-MoO₂ to α-MoO₃. *Opt. Mater.* **2011**, *33*, 480–484. [[CrossRef](#)]
47. Zhang, W.; He, Y.; Zhang, M.; Yin, Z.; Chen, Q. Raman Scattering Study on Anatase TiO₂ nanocrystals. *J. Phys. D Appl. Phys.* **2000**, *33*, 912–916. [[CrossRef](#)]
48. Suo, Z.; Kou, Y.; Niu, J.Z.; Zhang, W.Z.; Wang, H.I. Characterization of TiO₂-, ZrO₂- and Al₂O₃-Supported Iron Catalysts as Used for CO₂ Hydrogenation. *Appl. Catal. A Gen.* **1997**, *148*, 301–313. [[CrossRef](#)]
49. Mazza, T.; Barborini, E.; Piseri, P.; Milani, P.; Cattaneo, D.; Li Bassi, A.; Bottani, C.E.; Ducati, C. Raman Spectroscopy Characterization of TiO₂ Rutile Nanocrystals. *Phys. Rev. B* **2007**, *75*, 045416. [[CrossRef](#)]
50. Shrestha, A.; Gao, X.; Hicks, J.C.; Paolucci, C. Nanoparticle Size Effects on Phase Stability for Molybdenum and Tungsten Carbides. *Chem. Mater.* **2021**, *33*, 4606–4620. [[CrossRef](#)]
51. Gao, Q.; Zhao, X.; Xiao, Y.; Zhao, D.; Cao, M. A Mild Route to Mesoporous Mo₂C–C Hybrid Nanospheres for High Performance Lithium-Ion Batteries. *Nanoscale* **2014**, *6*, 6151. [[CrossRef](#)]
52. Zhu, Y.; Wang, S.; Zhong, Y.; Cai, R.; Li, L.; Shao, Z. Facile Synthesis of a MoO₂–Mo₂C–C Composite and Its Application as Favorable Anode Material for Lithium-Ion Batteries. *J. Power Sources* **2016**, *307*, 552–560. [[CrossRef](#)]
53. Ojha, K.; Saha, S.; Kolev, H.; Kumar, B.; Ganguli, A.K. Composites of Graphene–Mo₂C Rods: Highly Active and Stable Electrocatalyst for Hydrogen Evolution Reaction. *Electrochim. Acta* **2016**, *193*, 268–274.
54. Li, R.; Wang, S.; Wang, W.; Cao, M. Ultrafine Mo₂C Nanoparticles Encapsulated in N-Doped Carbon Nanofibers with Enhanced Lithium Storage Performance. *Phys. Chem. Chem. Phys.* **2015**, *17*, 24803–24809. [[CrossRef](#)] [[PubMed](#)]
55. Bhaskar, A.; Deepa, M.; Narasinga Rao, T.N. MoO₂/Multiwalled Carbon Nanotubes (MWCNT) Hybrid for Use as a Li-Ion Battery Anode. *ACS Appl. Mater. Interfaces* **2013**, *5*, 2555–2566. [[CrossRef](#)] [[PubMed](#)]
56. Chen, M.; Liu, J.; Zhou, W.; Lin, J.; Shen, Z. Nitrogen-Doped Graphene-Supported Transition-Metals Carbide Electrocatalysts for Oxygen Reduction Reaction. *Sci. Rep.* **2015**, *5*, 10389–10398.
57. Ji, W.; Shen, R.; Yang, R.; Yu, G.; Guo, X.; Peng, L.; Ding, W. Partially Nitride Molybdenum Trioxide With Promoted Performance as an Anode Material for Lithium-Ion Batteries. *J. Mater. Chem. A* **2014**, *2*, 699–704. [[CrossRef](#)]
58. Spevack, P.A.; McIntyre, N.S. A Raman and XPS Investigation of Supported Molybdenum Oxide Thin Films. 1. Calcination and Reduction Studies. *J. Phys. Chem.* **1993**, *97*, 11020–11030. [[CrossRef](#)]
59. Oshikawa, K.; Nagai, M.; Omi, S. Characterization of Molybdenum Carbides for Methane Reforming by TPR, XRD, and XPS. *J. Phys. Chem. B* **2001**, *105*, 9124–9131. [[CrossRef](#)]
60. Guil-López, R.; Nieto, E.; Botas, J.A.; Fierro, J.L.G. On the Genesis of Molybdenum Carbide Phases During Reduction-Carburization Reactions. *J. Solid State Chem.* **2012**, *190*, 285–295. [[CrossRef](#)]
61. Ma, Y.; Guan, G.; Hao, X.; Zuo, Z.; Huang, W.; Phanthong, P.; Kusakabe, K.; Abudula, A. Highly-Efficient Steam Reforming of Methanol over Copper Modified Molybdenum Carbide. *RSC Adv.* **2014**, *4*, 44175–44184. [[CrossRef](#)]
62. Su, X.; Yang, X.; Zhao, B.; Huang, Y. Designing of highly selective and high-temperature endurable RWGS heterogeneous catalysts: Recent advances and the future directions. *J. Energy Chem.* **2017**, *26*, 854–867. [[CrossRef](#)]
63. Zhu, M.; Ge, Q.; Zhu, X. Catalytic Reduction of CO₂ to CO via Reverse Water Gas Shift Reaction: Recent Advances in the Design of Active and Selective Supported Metal Catalysts. *Trans. Tianjin Univ.* **2020**, *26*, 172–187. [[CrossRef](#)]